"The g-2 laser calibration system: testing the light distribution chain"

Agnese Bonavita

Supervisor: Carlo Ferrari, Anna Driutti

Dipartimento di Fisica "E. Fermi" - Università di Pisa

Fermilab Summer School (25/07/16 - 23/09/16)

Contents

List of Figures

Abstract

A new experiment at Fermilab will measure the anomalous magnetic moment of the muon with a precision of 140 parts per billion (ppb). This measurement is motivated by the results of the Brookhaven E821 experiment that were first released more than a decade ago, which reach a precision of 540 ppb. The new Muon $(g-2)$ experiment will be equipped with a laser calibration system for all the 1296 channels of the calorimeters. My project during the summer internship concerned the construction an the data analysis of the light distribution chain. I had the opportunity to split my job in two parts: an hardware part and a software one. For the first one I have been involved in the assembly of the electromagnetic calorimeters by setting the optical components and preparing the fiber bundles subsequently connected to the panels with the fiber boxes and the diffusors. For the second one I took part to the data analysis of the Local Monitor (LM) that was under test during a recent test beam at SLAC laboratories. The main goal of my job was the baseline subtraction of the signals arriving to the LM in order to study the linearity of the response and the stability of the system.

Chapter 1

Introduction

1.1 The anomalous magnetic moment

The magnetic dipole moment $\vec{\mu}$ of an object is a measure of how much torque it experiences when placed in a magnetic field:

$$\vec{\tau} = \vec{\mu} \times \vec{B} \tag{1.1.1}$$

$$U = -\vec{\mu} \cdot \vec{B} \tag{1.1.2}$$

where U is the potential energy associated with the magnetic dipole moment. Subatomic particles of mass m and charge e have a magnetic moment that is generated by their intrinsic angular momentum, $\vec{S}$, these two quantities are related by the gyromagnetic factor g:

$$\vec{\mu} = g\left(\frac{e}{2m}\right)\vec{S} \tag{1.1.3}$$

The dimensionless number g is a fundamental property of the particle and its interactions. For the case of a simply rotating structure a particle which moves with speed v along a circular path or radius r, in the limit $r \longrightarrow 0$, the particle constitutes a loop that encloses an area $A = \pi r^2$ and carries a current $I = \frac{ev}{2\pi r}$. The magnitude of the magnetic moment is:

$$\mu = IA = \frac{evr}{2} \tag{1.1.4}$$

considering that $L = mvr$ we can write

$$\vec{\mu} = \left(\frac{e}{2m}\right)\vec{L} \tag{1.1.5}$$

Comparison shows that g = 1 using a purely classical treatment.

The breakthrough in the mathematical description of spin came in 1928 from Dirac's attempt to create a relativistic extension of Schrondinger's equation that, unlike the Klein-Gordon equation, preserved linearity respect to the time. Given the success in Quantum Mechanics in predicting g to be 2 for the half-integer spin electron, it was natural to assume that the half-integer spin proton would also be a Dirac particle with $g = 2$.

1.2 Muon properties

Why the muon anomalous magnetic moment is so interesting and plays a key role in elementary particle at its fundamental level is due to the fact that it can be predicted by theory with very high accurancy and at the same time can be measured as precisely in an unambiuguos experimental setup. The muon $g-2$ experiments observe the motion of the spin of the muons on circular orbits in a homogeneous magnetic field. This requires the muons to be polarized. After the discovery of the parity violation in weak interaction it immediatly became evident that weak decays of charged pions are producing polarized muons, thereby the maximal parity violation of charged current processes provides the ideal conditions. The point is that right-handed neutrinos ν_R are not produced in the weak transitions mediated by the charged $W^{\pm}$ gauge bosons. Consequently the production rate of ν_R's in ordinary weak reactions is pratically zero which amounts to lepton number conservation for all pratical purposes in laboratory experiments.
Pions may be produced by shooting protons (accumulated in a proton storage ring) on a target material where pions are the most abundant secondary particles. The most effective pion production mechanism proceeds via excitation and subsequent decay of baryon resonances.
The muon g-2 experiment is based on the decay chain

$$\pi \longrightarrow \mu + \nu_\mu \tag{1.2.1}$$

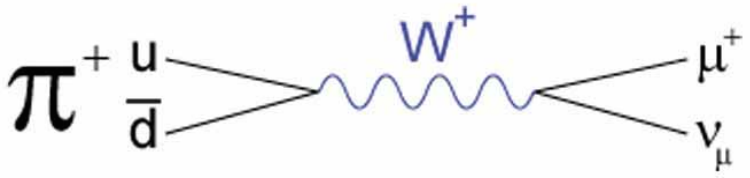

Figure 1.2.1: π-decay

producing the polarized muons which decay into electrons which carry along with their direction of propagation the muon's polarization.
Let's consider, for example, the π^+ decay. Being a two body decay, the lepton energy is monochromatic and given by

$$E_\mu = \sqrt{m_\mu^2 + p_\mu^2} = \frac{m_\mu^2 + m_\pi^2}{2m_\pi^2}, \quad p_\mu = \frac{m_\mu^2 - m_\pi^2}{2m_\pi^2} \tag{1.2.2}$$

Since the π^+ has spin 0 and the emitted neutrino is left-handed, by angular momentum conservation along with the left-handed helicity state of the neutrinos, the μ^+ must be left-handed as well.
Because of the spin-zero nature of the pion, the decay muons are emitted isotropically. Hence a pion source produces an unpolarized muon distribution. The helicity discussion implies that for any positive muon, the spin is anti-parallel to the momentum. Thus, to an observer with a small solid angle view of a pion source, muons are highly polarized. This is exactly the case for muons that are guided from a pion source to an experiment using a beamline.
The muon is unstable and decays via the weak three body decay:

$$\mu^+ \longrightarrow e^+ + \nu_e + \overline{\nu}_\mu \tag{1.2.3}$$

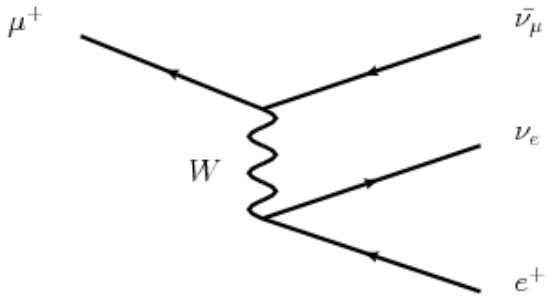

Figure 1.2.2: μ-decay

The μ^+ ant the e^+ would be right handed in the massless approximation. This implies the decay scheme of the muon (Fig. 1.2.3) Again it is the P violation which prefers

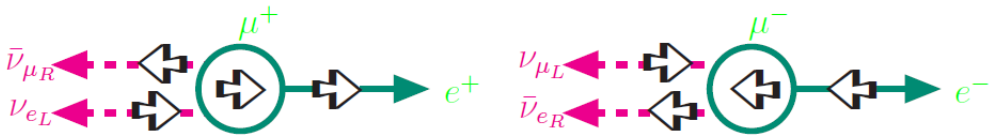

Figure 1.2.3: In $\mu^\pm$ decay the produced $e^\pm$ has positive [negative] helicity, respectively

positrons (electrons) emitted in the direction or the muon spin (opposite to the muon spin). Therefore, the measurement of the direction of the positron (electron) momentum provides the direcion of the muon spin (opposite to the muon spin).

Chapter 2

The Muon g-2 Experiment

2.1 Overview and main goals of the experiment

The measurement of a_μ in principle is very simple. As illustrated in figure, when polarize muons travel on a circular orbit in a costant magnetic field, then a_μ is responsible for the Larmour precession of the direction of the muon spin, characterized by the angular frequency $\vec{\omega}_a$. Correspondingly, the principle of the BNL muon $g-2$ experiment involves the study or the orbital and spin motion of highly polarized muons in a magnet storage ring. This method has already been applied in the last CERN experiment. The key improvements of the BNL experiment include the very high intensity of the primary proton beam from the proton storage ring AGS (Alternating Gradient Synchrotron), the injection of muons instead of pions into the storage ring and a super ferric storage ring magnet. Protons of energy 24 GeV from the AGS hit a target and produce pions. The pions are unstable and decay into muons plus a neutrino, as shown in fig.1.2.1 where the muons carry spin and thus a mangetic moment which is directed along the direction of the flight axis. The longitudinally polarized muons from pion decay are then injected into a uniform magnetic field $\vec{B}$ where they travel in a circle. The ring is a toroid-shaped structure with a diameter of 14 meters, the aperture of the beam pipe is 90 mm, the field is 1.45 T and the momentum of the muon is $p_\mu = 3.094$ GeV. In the horizontal plane of orbit the muons execute a relativistic cyclotron motion with angular frequency ω_c. By the motion of the muon magnetic moment in the homogeneous magnetic field the spin axis is changed in a particular way as described by the Larmor precession. The muon spin is processing with angular frequency ω_s, which is slightly bigger than ω_c by the difference angular frequency $\omega_a = \omega_s - \omega_c$.

$$\omega_c = \frac{eB}{m_\mu \gamma}, \omega_s = \frac{eB}{m_\mu \gamma} + a_\mu \frac{eB}{m_\mu}, \omega_a = a_\mu \frac{eB}{m_\mu} \tag{2.1.1}$$

where $\gamma = \sqrt{1-v^2}$ is the relativistic Lorentz factor and v the muon velocity. In the experiment ω_a and B are measured. The muon mass m_μ is obtained from an experiment on muonium, which is a $(\mu^+ e^-)$ bound system. Note that if the muon just has its Dirac magnetic moment $g = 2$ the direction of the spin of the muon would not change at all.
In order to retain the muons in the ring an electrostatic focusing system is needed. Thus in addiction to the magnetic field $\vec{B}$ an electric quadrupole field $\vec{E}$ in the plane normal to the particle orbit must be applied. This transversal electric field changes the angular frequency according to

$$\vec{\omega_a} = \frac{e}{m_\mu}\left(a_\mu \vec{B} - \left[a_\mu - \frac{1}{\gamma^2 - 1}\right]\vec{v} \times \vec{E}\right) \tag{2.1.2}$$

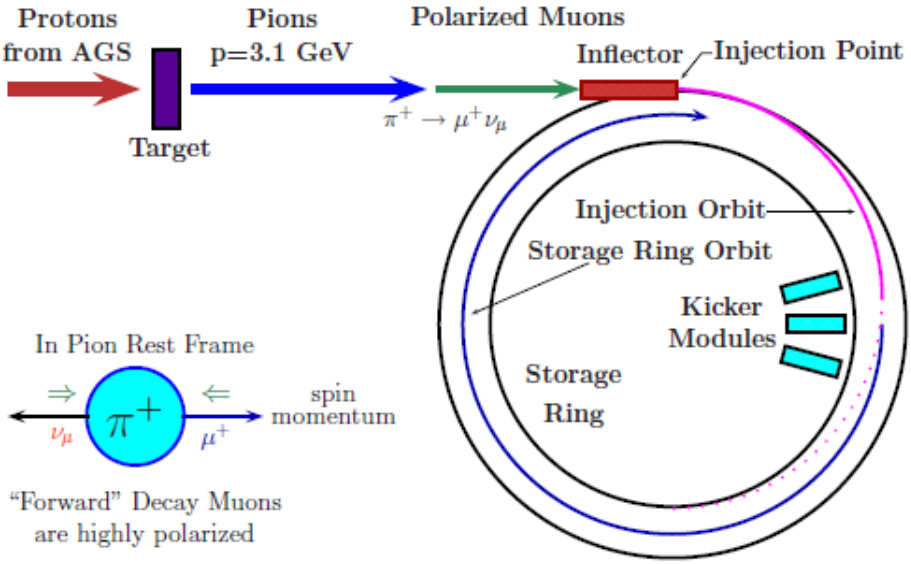

Figure 2.1.1: The schematics of muon injection and storage in the $g-2$ ring.

This key formula for measuring a_μ was found by Bargmann, Michel and Telegdi in 1959. Interestingly,one has the possibility to choose γ such that $a_\mu - 1/(\gamma^2 - 1) = 0$, in which case ω_a becomes independent of E. This is the so–called *magic* γ. When running at the corresponding magic energy, the muons are highly relativistic, the magic γ-factor being $\gamma = 1 + 1/a_\mu = 29.3$. The muons thus travel almost at the speed of light with energies of about $E_{magic} = \gamma m_\mu \simeq 3.098$ GeV. This rather high energy, which is dictated by the requirement to minimize the precession frequency shift caused by the electric quadrupole superimposed upon the uniform magnetic field, also leads to a large time dilatation.The lifetime of a muon at rest is 2.19711μs, while in the ring it is 64.435μs (theory) [64.378μs (experiment)]. Thus, with their lifetime being much larger than at rest, muons are circling in the ring many times before they decay. In this decay we have the necessary strong correlation between the muon spin direction and the direction of emission of the positrons.

As the corrisponding Standard Model predictions have been refined, the experimental and theoretical values have persistently differed by about 3 σ.
While it is not yet definitive, the discrepancy strongly suggests that there may be effects on the muon's magnetic moment from particles or interactions that are not included in the Standard Model. The Dirac equation predicts that $g = 2$, so since $a_\mu = (g-2)/2$, a nonzero value for a_μ arises from coupling to virtual particles. The vast majority (99.6%) of the value of a_μ arises from the leading-order quantum electrodynamics (QED) process that involves the exchange of a single virtual photon, and higher-order QED contributes nearly all of the rest.
Parity violation causes the high-energy positrons produced in μ^+ decay to preferentially follow the muon spin direction(see fig. 1.2.2 and fig. 1.2.3), so the number of positrons

that are detected by electromagnetic calorimeters with energy above a defined threshold is modulated at ω_a. The anomalous magnetic moment is then calculated as

$$a_\mu = \frac{R}{(\lambda - R)} \tag{2.1.3}$$

where $R = \omega_a/\omega_p$, ω_p is the proton Larmor precession angular velocity and $\lambda = \mu_\mu/\mu_p$. The magnetic field is provided by a circular magnet that has a C-shaped cross section and consists of a steel yoke and precisely ground pole pieces that are excited by four superconducting niobium-titanium coils; it operates at a field of magnitude 1.45 T.

The error achieved by the BNL E821 experiment was 0.54 ppm. The greater than 3σ difference found by E821 with respect to the theoretical expectation, was limited and does not meet the 5σ threshold for claiming a discovery, so a more precise measurement is needed to rule out statistical fluctuations and confirm the discrepancy. The goal of the g-2 experiment at Fermilab is a four-fold improvement in the experimental precision thereby reducing the error on a_μ up to 0.14 ppm which is comparable to the 0.4 ppm uncertainty on the most accurate Standard Model prediction. While BNL E821 improved on the CERN III experiment in a revolutionary manner, primarily by the invention of direct muon injection into the storage ring, the FNAL E989 experiment will introduce a broad suite of refinements focused on optimizing the beam purity and rate and modernizing the instrumentation used to measure both ω_a and ω_p.
E989 will use the same muon storage ring of E821, which has been relocated to Fermilab in a new building characterized by mechanical stability and controlled temperature. Many improvements are needed with respect to the previous experiment to reach the statistical uncertainty of 0.1 ppm as requested.
One of the most important concerns the pion decay line: a limiting factor at BNL was the 120 m beamline between the pion production target and the storage ring; because the decay length of a 3.11 GeV/c pion is $\approx$ 173 m, the beam injected into the storage ring contained both muons and a significant number of undecayed pions, the latter creating an enormous burst of neutrons when intercepting materials: their subsequent capture in scintillator-based detectors impacted detector performance adversely. E989 will use a 900m pion decay line to reduce this background.
Moreover the detectors and electronics will all be newly constructed to meet the demands of measuring the spin precession of the muon to a statistical error of 0.1 ppm, while controlling systematics on ω_a to the 0.07 ppm level; this is a substantial improvement over the E821 experiment. Better gain stability and corrections for overlapping events in the calorimeters are crucial improvements addressed in the new design.
A new tracking system will allow for better monitoring of the stored muon population, thus improving the convolution of the stored muon population with the magnetic field volume, and establishing corrections to ω_a that arise from electric field and pitch corrections

2.2 The calorimeter system

The new Muon $(g-2)$ experiment at Fermilab improves the BNL experiment in many aspects.One of them concerns the new calorimeter system composed by 24 electromagnetic calorimeter stations placed on the inside radius of a magnetic storage ring. The detector must accurately measure the hit times and energies of the positrons, which curl to the inside ring following the muon decay.

For maximum acceptance, the calorimeters are located partly within the storage ring's hightly uniform 1.45 T magnetic field and extend inward radially to a region where the field falls to ≈ 0.8 T. A calorimeter station will consist of 54 lead fluoride (PbF_2) crystals in a 6 high by 9 wide array, with each crystals read out on the rear face using a large area SIPM coupled directly to the crystal surface. While PbF_2 calorimeters have not been extensively used in the past, their properties are particularly well suited to the needs of the Muon $g-2$ experiment: PbF_2 has very high density (7.77 g/cm^3), a 9.3 mm radiation lenght and a Molière radius of $R_M^E = 22$ mm for energy deposition. The relatively new developement of SiPMs as light transducers has considerable advantages compared to PMT's, although with several distinct challenges. Their compact nature provides freedom in the mechanical design of the calorimeter housing so they can be mounted in tight geometries. They operate in high magnetic fields without degradation and they do not perturb the magnetic field as long as a suitable choice of the electronics support components is made. It is also necessary that the detectors preserve a temperature and bias control stability during operation.
The response of each of the 1296 channels must be calibrated and monitored to keep uncertainties due to gain fluctuations at the sub-permil level in the time interval corresponding to one beam fill ($\sim 700\mu$s).
On longer timescale, the goal is to keep systematic contributions due to gain fluctuations at the sub-percent level. In Fig. 2.2.1 we can see all the detection process of the particles.

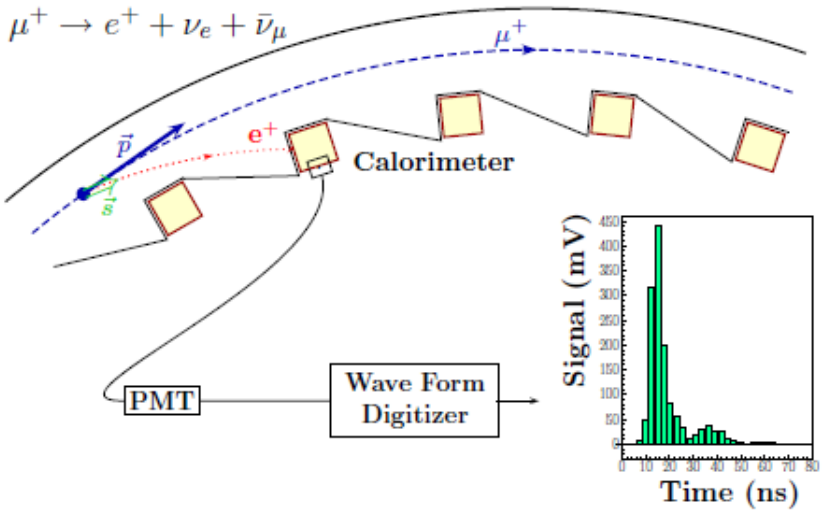

Figure 2.2.1: Detection process

Chapter 3

The calibration system for the g-2 calorimeters

3.1 Purpose of the calibration system

Calibration of the almost 1300 channels has to be performed during data taking. The proposed solution is based on the method of sending simultaneous light calibration pulses into the SiPMs throught the active crystals that make up the calorimeters. Light pulses should be stable in intensity and timing in order to correct systematic effects due to drifts in the response of the crystal readout devices.
A suitable photo-detector system must also be included in the calibration architecture to monitor any fluctuations in time of the light source intensity and beam pointing as well as any fluctuation of the trasmitted light along the optical path of the light distribution system.
Some guidelines are defined to select the light source and to design the geometry of the light distribution and monitoring; the following criteria are adopted to select the light source type:

- light wavelenght must be in the spectral range accepted by the detector and determined by the convolution of the spectral density of the Cherenkov signal produced by electrons in PbF_2 crystals with the transmission of the crystals and the quantum efficiency of the SiPM;

- the luminous energy of the calibration pulses must be in the same range or that produced by the conversion or the electron energy in the crystals, typically 1-2 GeV, into light. If we take, for the number of laser photons per pulse the value $N_\gamma \sim 2 \cdot 10^4$ of Cherenkov photons integrated by a PMT. The laser equivalent energy pulse on each tower is almost:

$$E_{pulse}^{crystal} = N_\gamma \times E_\gamma = N_\gamma \times h\frac{c}{\lambda} = 2{\cdot}10^4 \times 6.6{\cdot}10^{-34}\text{J}{\cdot}\text{s} \times \frac{3 \cdot 10^8 \text{m/s}}{400 \cdot 10^{-9}\text{m}} = 0.01\text{pJ} \quad (3.1.1)$$

- the pulse repetition rate must be of the order of 10 kHz; this value will be tuned to obtain the best compromise between the need of having enough calibration statistics in the time interval when the maximum rate is achieved in the redout devices and the need to avoid pileup.

Among many different types of pulsed lasers commercially available, pulsed diode lasers in the blue seem to best address all the criteria listed above and are considered as a source for the calibration pulses.
The laser source fully agrees to all the guidelines defined by the experiment:

Wavelenght	405± 10 nm
Pulse FWHM	700 ps
Avarage Power (at 40 MHz)	28 mW
Measured light output	1000 pJ/pulse at 10 kHz

Table 3.1.1: Properties of the laser source

Two time scales, related to gain fluctuations, are be monitored:

- short term fluctuations ($0 - 700\mu$s: time of a fill): this kind of fluctuations is not related to environmental factors but rather to beam features such as muon rate, incoming electrons which can cause over/under voltages; the calibration has to be performed online, using laser pulses during the fill;
- long term fluctuations (hours/days): this kind of fluctuation does not depend on the beam but rather on local factors such as drift day/night, temperature, bias voltage variations; the calibration can be performed offline: it has to be checked when the system goes beyond a threshold value upon which measurement perturbations are evident.

3.2 Set-up of the calibration system

The guidelines for designing the light distribution chain are:

- high sensitivity monitors of the transmitted light at the end-point of each individual section of the distribution chain must be used to ensure online control of the system stability and to have infomation to apply feedback corrections to the source operation parameters, if needed;
- the optical path must be minimized in order to limit the light loss due to self-absorption in the optical fibers; the number of cascade distibution points must be also minimized to reduce the unavoidable light loss in the couplers between different sections;
- the laser source and its control electronics should be located outside the muon ring in order to avoid electromagnetic perturbations of the local field induced by the current flow used to excite the laser;
- optical fiber selection: quartz fibers are the best solution for long path light transmission and in terms of robustness against solarization or other effects due to large values of transmitted light intensity.

The task of the distribution chain is to divide and carry the light from the laser source to the different calorimeter stations placed around the ring, preserving as much as possible

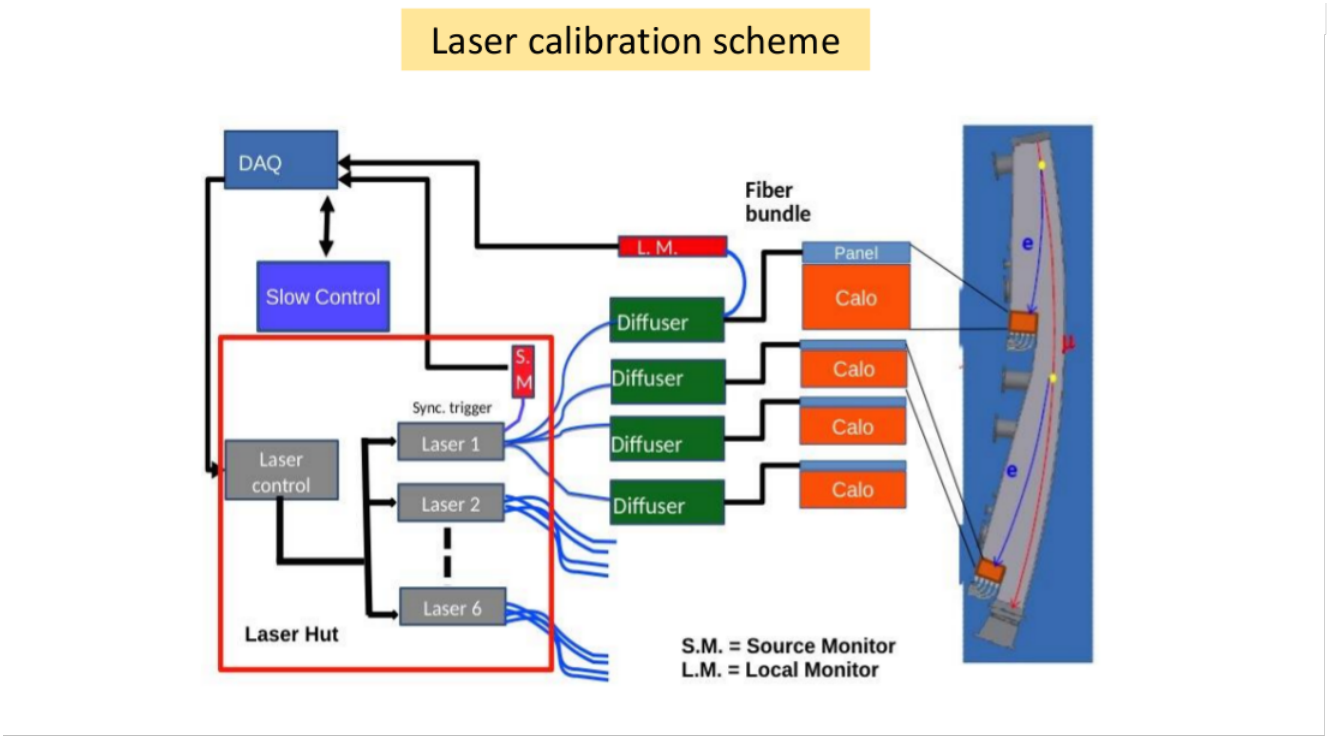

Figure 3.2.1: Key elements of the laser calibration system: multilaser with 6 heads, 24 launching fibers, 24 diffuser, 6 source monitors and 24 local monitors.

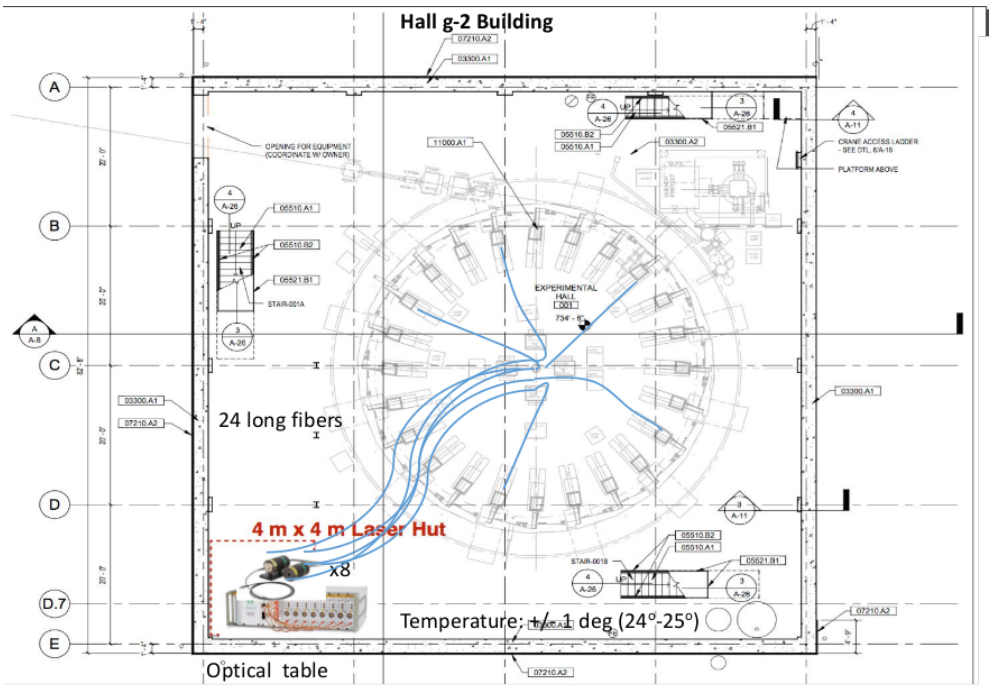

Figure 3.2.2: $g-2$ experimental hall

uniformity and intensity of the laser light source.
The first step consist in collecting the light of the laser using optical fibers. The attenuation loss of the fibers should be minimized because the laser will be placed in the Laser Hut$\sim$ 25 m far away from a single calorimeter station. For this reason the fibers used are quartz fibers with an attenuation of 5 dB/km at 400 nm (see Fig. 3.2.1 and Fig. 3.2.2). Each laser is splitted in four and coupled to quartz fibers. To connect all the equipment with the engineered diffuser, which is the item placed near the calorimeter, a 25 m long launching fiber is used. The diffuser is then coupled, throught a 0.5 m fiber bundle, to the front panel placed in front of the crystals. One of the major efforts or the distribution chain is related to the design and the construction of the front panel, necessary to couple the fibers coming from the diffuser to the calorimeter.This front panel has 6x9 holes. Each hole houses a 8×8 90° prism glued to the panel. Each fiber comes from one side and reaches every prism following guiding grooves starting on one side. A sketch of the sutup is presented in figure 3.2.3:

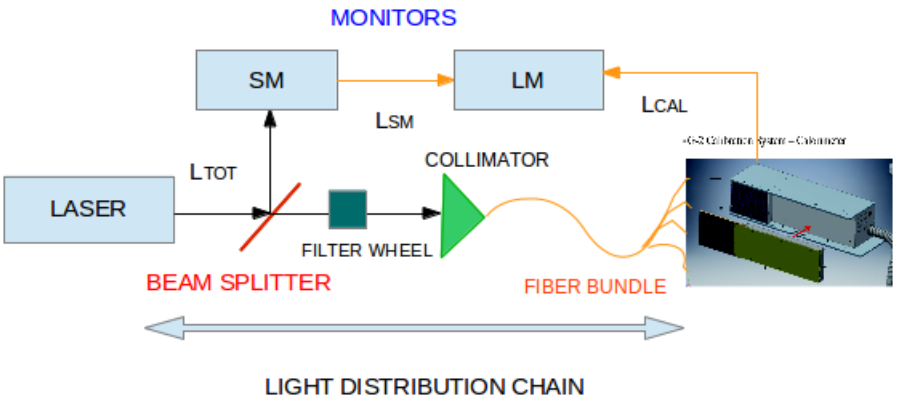

Figure 3.2.3: Setup of the calibration system

During the summer internship I have been involved in the construction of the light distribution chain. The assembly of the hardware part of the calibration setup was mainly done in a laboratory inside the D0 building. The first task I performed was cleaning all the panels from dust and residual materials. Panel were made of Delrin and, as shown in figure 3.2.4 , had spaces to allocate fibers and prisms. When panels were cleaned I filled them with the 54 right-angle prisms. Then I focused my attention to the optical components. I set the beam splitter (see figure 3.2.5 (a)): little cubes made from two triangular glass prism which are glued together used for split the light beam in two regardless the polarisation of the beam. In addition I set the collimators into the calorimeter boxes: these devices are used to collimate the laser beam into the optic fiber. The picture (fig 3.2.5 (b)) shows the collimator len, while the fiber it will be linked on the back.

During the second month of my internship I also took part to the fibers preparation. With the help of my supervisor and an other summer student (Alessia Renardi) I cut and clean the fibers. In some PVC tubes we inserted 4 fibers: two plastic fibers and two quarz fibers. A quarz fiber (yellow tube in figure 3.2.6 (a)) will be employ to transfer the laser light to the calorimeter. The other three (the blue quarz fiber and the plastic ones) carry the light from the Local Monitor to the panels. We decided to use two different type of fibers because we hope to reward the transmission coefficient variations due to

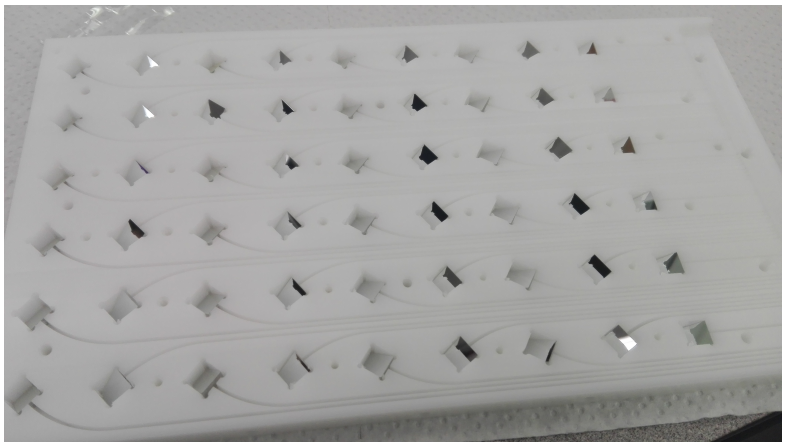

Figure 3.2.4: One of the panel filled with the crystals

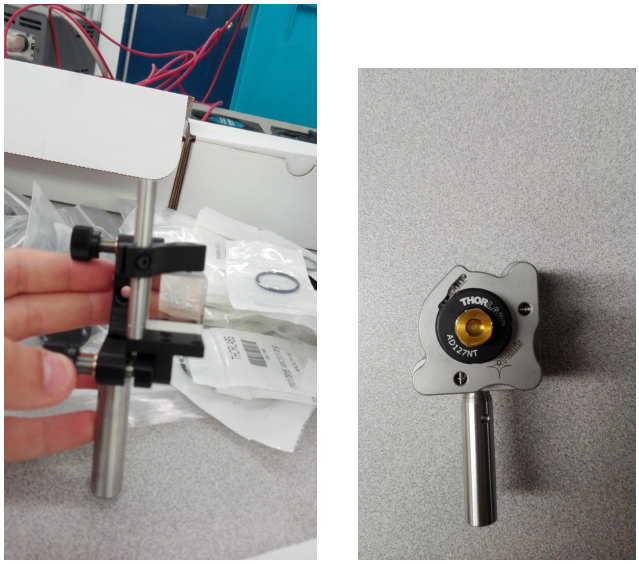

(a) (b)

Figure 3.2.5: From the left: a beam splitter (a) and a collimator (b) assembled

temperature instability. In future more test to compare the quality of the two kind of fibers will be made.
Moreover I assembled the fibers bundles and I helped my supervisor to connect and put together all the components previously assembled to the panels with the fiber boxes and the diffuser tubes. In figure 3.2.6 (b) is shown the result of this operation. After that we also tested the power of every fiber of the bundle in order to verify the right working of each fiber (we were looking for an average power of $\sim 4\mu$W).

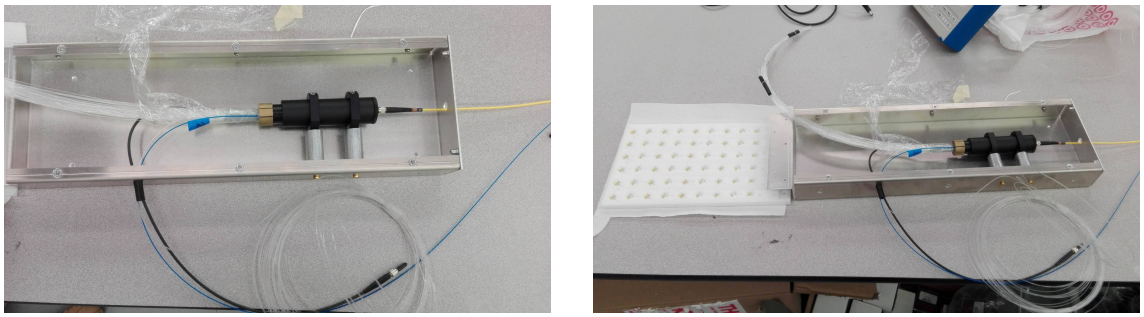

(a) (b)

Figure 3.2.6: Optic chain definitively assembled

Chapter 4

Testing the light distribution chain

4.1 Introduction to the analysis

The most important feature of the calibration system is light stability. In fact it is requested by the experiment a stability of the order of 10^{-4} over 2 hours. To be sure that this level of stability is maintained during data taking a monitoring procedure has to be included in this calibration system. The monitoring system is composed of two parts: a Source Monitor (SM) and a Local Monitor (LM). The Source Monitor checks all the possible fluctuations of the laser sources. The number of Source Monitors is the same of the laser sources. The Local Monitor checks the stability of the light in the distribution chain.
Temperature stability is extremely important too: the gain of SiPMs is significantly sensitive to temperature variations of less than 0.1C. SiPMs temperatures will be monitored and the temperature inside the experimental hall will be maintained stable and uniform as much as possible.

Part of my job during this summer school concerned the analysis of the Local Monitor data that was under test during a recent test beam. In the next section the details of what is the LM and what is used for are described.

4.2 The Local Monitor

In order to closely monitor the light that illuminates each of the channels and diagnosing the source or eventual instabilities in the distribution system a Local Monitor has been devised. The system under test consists of a custom made detector assembly based of photomultiplier tube (PMT) placed 25 metres far away from a prototype of calorimeter station.
As shown in figure 3.2.3, the monitor receives two different signals with two pulses separated in time by approximately 250 ns. The first signal (L_{SM}) is light from the SM while the second (L_{CAL}) comes directly from the fiber bundle placed near the calorimeter. The monitoring system is also equipped with a Filter Wheel (FW), whose consist of a set of filters with different transmission factor. The FW is essential for checking the linearity in the response of the PMT and to quote the light as number of photoelectrons detected by the PMT (photoelectron statistics calibration). The advantage of this setup is that the ratio of the pulses, L_{CAL}/L_{SM} is a direct measurement of the fluctuations in the light chain independent of gain and laser fluctuation (these effects cancel out when the ratio

L_{CAL}/L_{SM} is performed). In figure 4.2.1 is possible to see the initial conditions of the pulses that arrive to the LM.

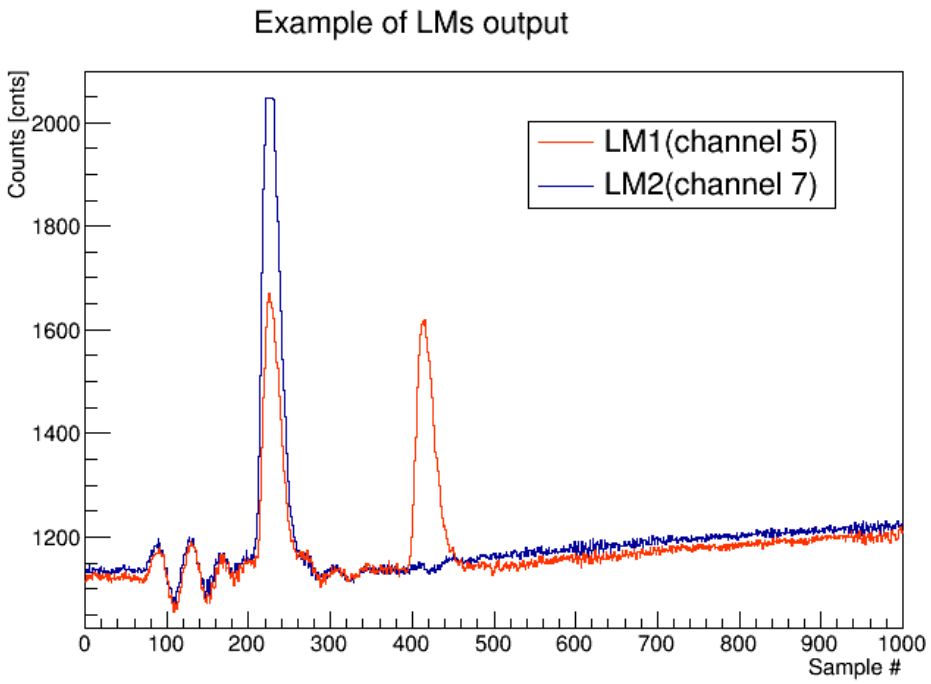

Figure 4.2.1: A tipical LM event

From fig. 4.2.1 is well visible that, beside the common baseline noise typical of the ADC-converters, an electronic noise contributes to the background. The same noise was picked up by another PMT that collected only the L_{SM} light (blue line). Subtraction of these two contributions was the challenged of the analysis. In order to optimize the best results I focused on a set of runs from 1751 to 1758 and I tried different ways to reduce and remove the baseline plus noise from the signal.

The runs I choose to analyze are the so called "calibration runs". Each of these runs collected events with a different filter setting so that the light of the second pulse has different intensities, see figure 4.3.3. This choice allowed to check the linearity in response and to perform a calibration trough the photoelectron statistics. Since the electronic noise influences the results of these two measurements, I used them as figure of merit to decide which method allows the best background rejection.

4.3 Analysis of the calibration runs

The first idea was using the trace of the other LM (LM2, green line in 4.2.1) to subtract the baseline by performing a bin by bin subtraction between the two lines. The procedure used was the following: first of all I removed the LM2 single peak (the blue line in figure 4.3.1) then I fit the corresponding interval with a linear function and replaced the histogram with the fit function (red line in Fig.4.3.1).

After that I subtracted bin by bin the red curve from the green curve. The plot I obtained is shown in figure 4.3.2.

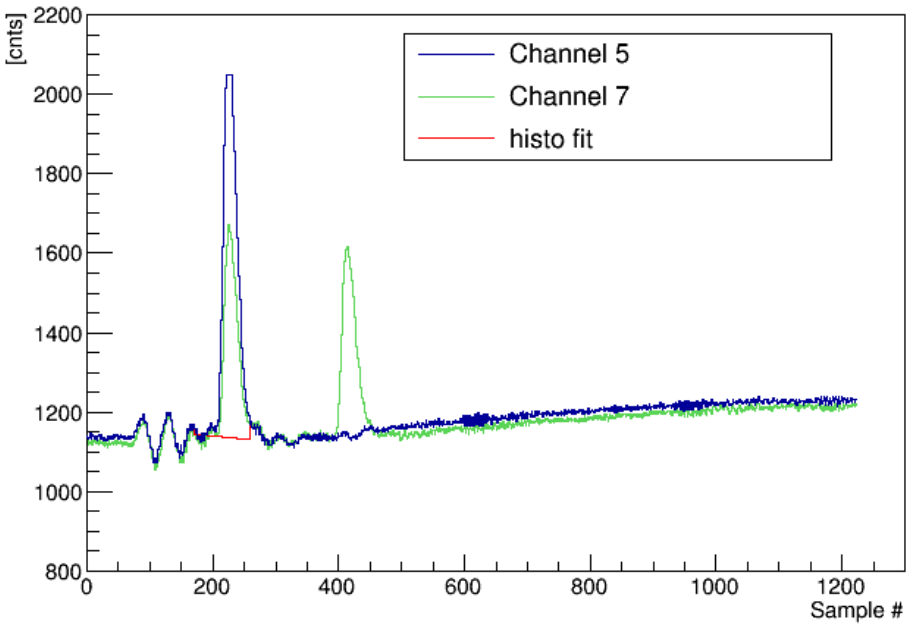

Figure 4.3.1: Removing the baseline: the red line represents the fit function

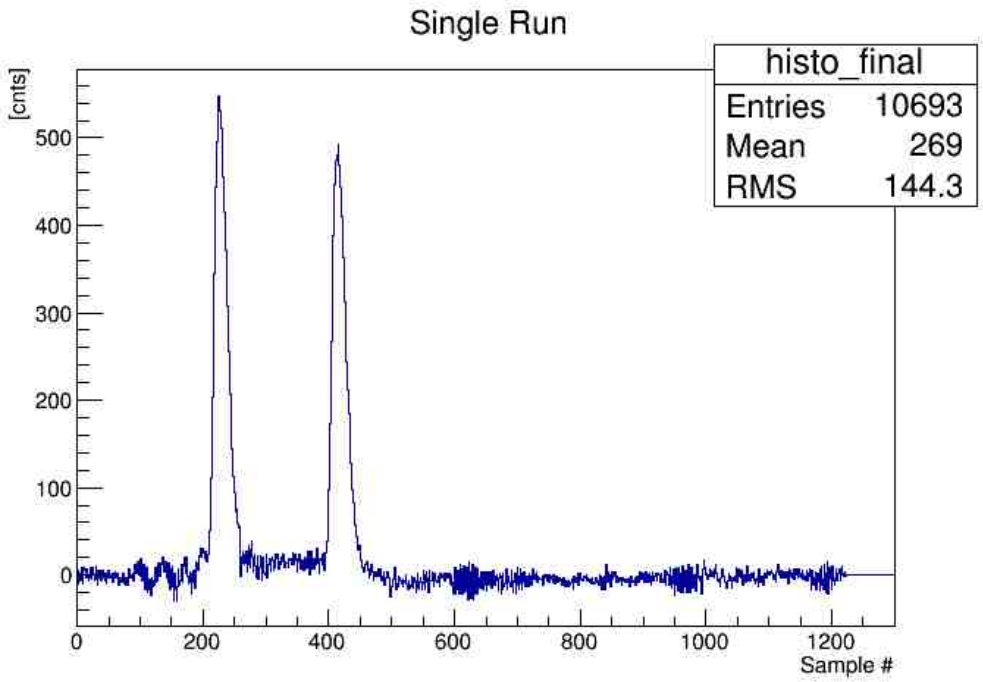

Figure 4.3.2: First result of the baseline subtraction

Then, I calculated the areas below the peaks (I set the integration interval and I used the same for all the runs, see figure 4.3.4). We expect that peak's integrals are proportional to the charge collected in the PMT. In a second time I tried to do the same by analyzing the two peaks separately and by subtracting to each of the two peak histograms the mean of the first 80 bins in order to remove the baseline. After that I just follow the same

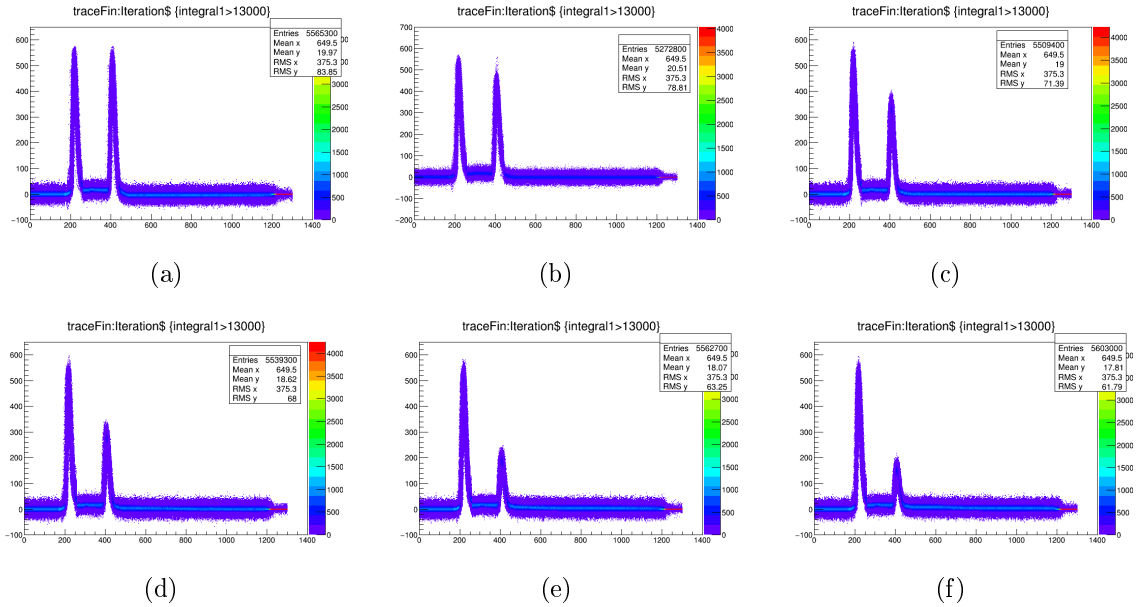

Figure 4.3.3: persistency plots of the runs.

procedure and I used the peaks areas for the calibration analysis.

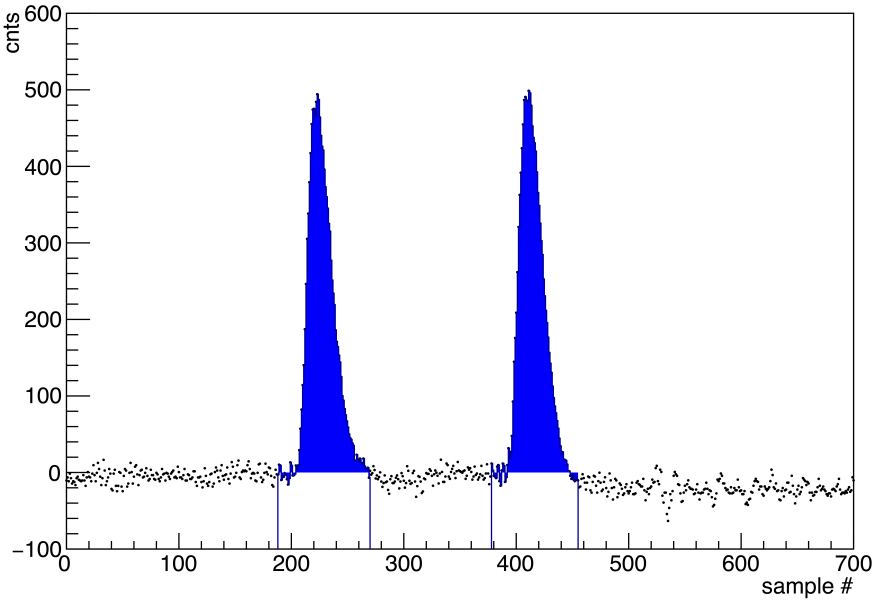

Figure 4.3.4: FIRST METHOD: an integration around the peaks with a fixed range

In any case the best idea that we had is the baseline subtraction using a template event-per-event. I considered the channel 7 and channel 8. Channel 7 represent LM2 output (so it has the same noise of LM1's signal) while channel 8 is just noise. I made the template by removing the LM2 single peak and replacing it with the channel 8 signal and I performed a subtraction. An example of the baseline template is shown in Fig 4.5(a), while the resul of the subtracion is shown in Fig 4.5(b).

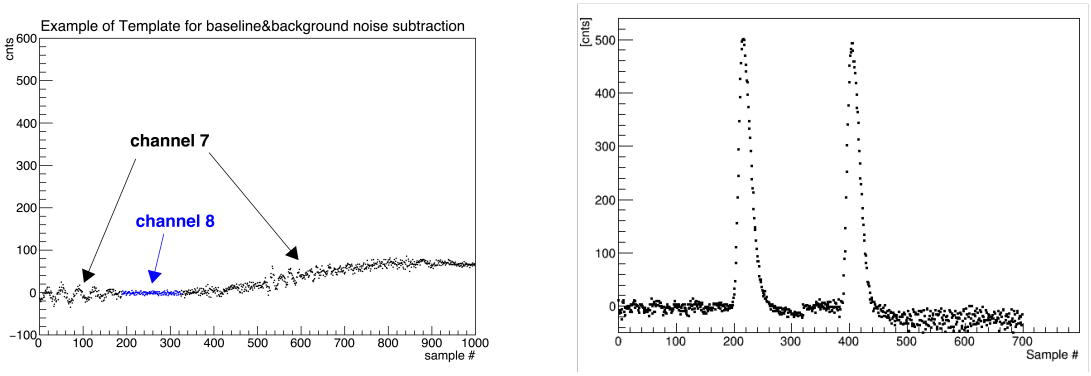

(a) (b)

In this case to evaluate the charge of the signal we performed a fit with the template T(x). The template function was given to me, but I knew it was data-driven by averaging events of an independent run. The fit function that we choose is a 3 parameters function, $p_0 T(x+p_1) - p_2$ where p_0 is the scale, p_1 is the peak position and p_2 is the baseline value after the subtraction. I did the fit twice, one for each pulse. Fit performance is shown in Fig. 4.3.5. The advantage of this method is that residual baseline and noise are excluded.

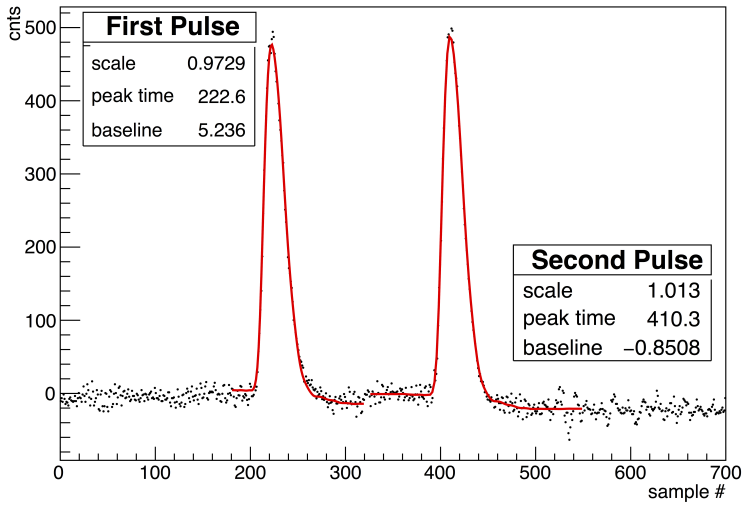

Figure 4.3.5: SECOND METHOD: template fit

Finally I used the calibration runs to check the linearity of the PMTs. For each run I fit with a Gaussian function the distribution of the second peak integral and I plotted the mean value extracted by the fit parameters versus the transmittance[1] (previously measured by my supervisor Carlo Ferrari).
The plots I obtained is shown in figure 4.3.6.

[1]The transmittance is the fraction of incident electromagnetic power that is transmitted through a sample, in contrast to the transmission coefficient which is the ratio of the transmitted to incident electric field

As we can see the two plots are very similar and the results with the two methods are compatible: the parameters value are the same within uncertainties.

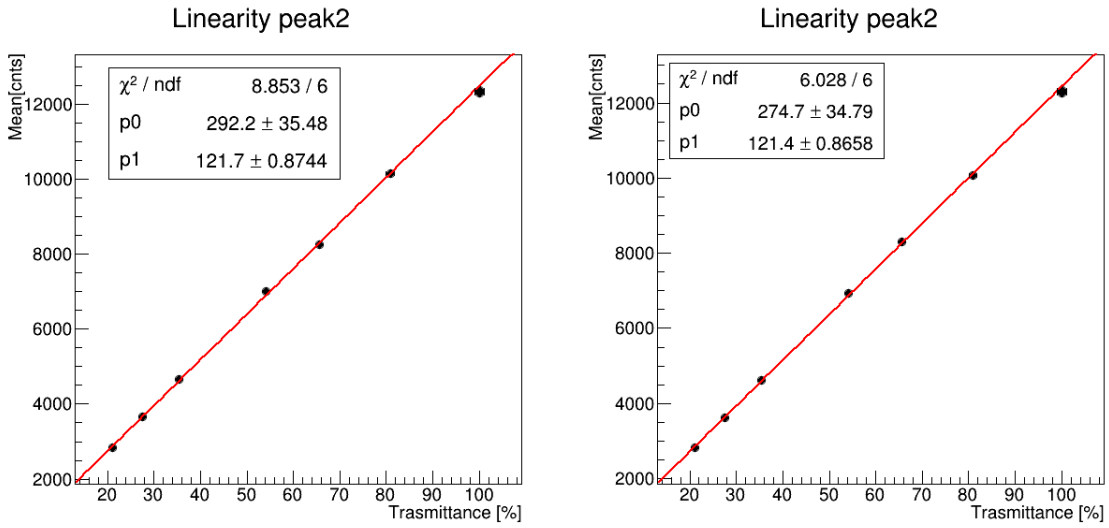

(a) (b)

Figure 4.3.6: Linear response of the PMT using the integral calculation of the two peaks (a) and using the template fit (b).

4.3.1 Photocalibration

Since the PMT response is linear, the PMT signal is expected to be proportional to the number of photoelectrons, $n_{p.e}$:

$$(\mu - \beta) = k\langle n_{p.e}\rangle \tag{4.3.1}$$

where μ is the mean of the PMT pulse integral distribution, after the baseline subtraction β; the signal variance is the sum of photoelectrons statistics term, $\sigma^2_{p.e}$, an electronic noise contribution, σ^2_e, and the intrinsic laser pulse fluctuations, $\sigma^2_L = (\alpha k(\mu-\beta))^2$, where α is the average relative laser intensity variation, which has been measured to be less than 1%.

$$\sigma^2 = \sigma^2_{p.e} + \sigma^2_e + \sigma^2_L \tag{4.3.2}$$

Since the p.e. component follows the Poisson statistics, assuming a statistical indipendence of the three sources of fluctuations, the dependance of σ^2, as a function of the measured light intensity is given by:

$$\sigma^2 = k^2\langle n_{p.e}\rangle + \sigma^2_e + \sigma^2_L = k(\mu-\beta) + \sigma^2_e + q(\mu-\beta)^2 \tag{4.3.3}$$

The proportional factor k can be obtained by fitting with a pol2 function σ^2vs $(\mu-\beta)$, and is the conversion factor from pulse integral (measured in ADC counts) and photoelectrons seen by the PMT.
Therefore, I obtained the conversion factor from pulse integrals to photo-electrons by fitting the variance vs mean curve as shown in figure 4.3.7.

The quadratic parameter (p_2) is a statistically significant contribution proportional to the signal, the linear parameter (p_1) is the conversion factor while p_0 is due to electronic noise.

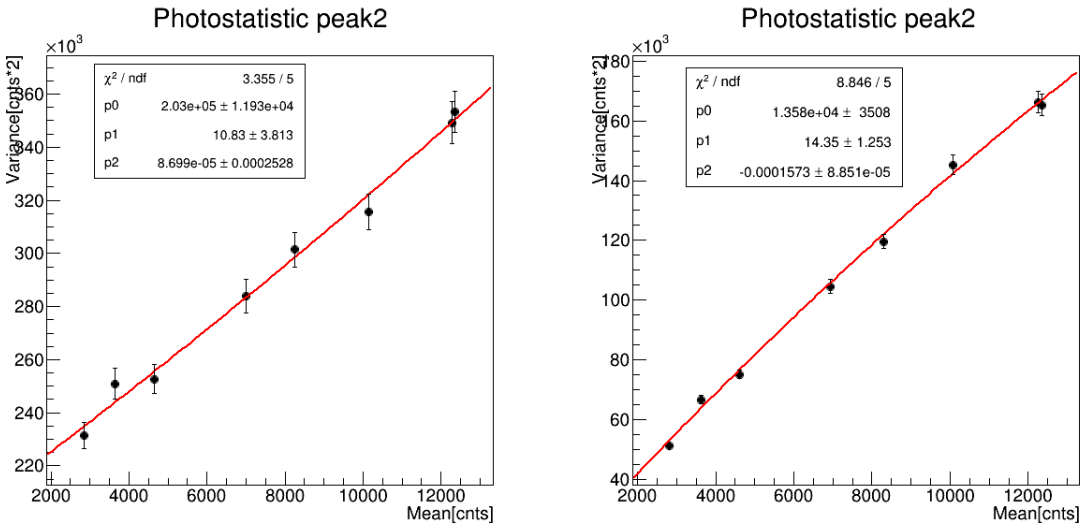

(a) (b)

Figure 4.3.7: Photostatistic calculated by the integration of the two peaks (a) and by template fit (b). At max (no filters) we measured 910 p.e and 870 p.e respectively.

By using this factor we measure that when the filter has 100% of trasmittance the p.e. are $N_{p.e} = \mu/k = 12500/14 \sim 900$ p.e. which correspond to an expected resolution of $1/\sqrt{N_{p.e.}} = 3.3\%$ per pulse. Also in this case the results achieved with the two methods are similar.

4.3.2 Timing

An important characteristic of the system is the time between the two pulses. We can extimate the time distance between the signals considering the fibers lenght (L) and their refrection index (n). In the Muon $g-2$ experiment quarz and plastic fibers will be used. As shown in figure 4.3.8 the distance between the LM and the SM is almost 2 metres while the lenght of the fiber that links together collimator, calorimeter and LM is almost 50 metres long. Knowing that $v = \frac{c}{n}$ where $c = 0.3$ m/ns, while $n_{quarz} = 1.475$ and $n_{plast} = 1.49$ we obtain:

$$\Delta_T(SM - LM) \sim \frac{2}{0.3/1.49} \simeq 10 \text{ ns} \tag{4.3.4}$$

$$\Delta_T(collimator - calorimeter - LM) \sim \frac{25}{0.3/1.475} + \frac{25}{0.3/1.49} \simeq 122.9 + 124.2 \simeq 247.1 \text{ ns} \tag{4.3.5}$$

Therefore, the expected time difference between the two signal arriving to the LM is $\simeq$ 237 ns. In the plot that I obtained, shown in figure 4.3.9 , the mean value is $\sim$ 235 ns. The discrepancy is compatible with the approximations that I made during the calculation but it is acceptable for the purpose. Figure 4.3.9 also shows that the time distribution obtained using the fit (peak's time is a free parameter of the fit) and the

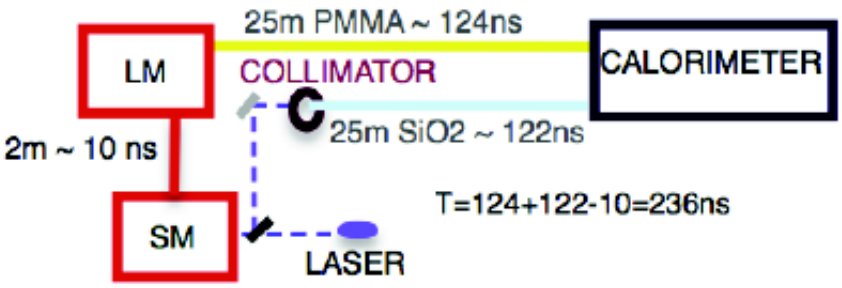

Figure 4.3.8: Setup of the light distribution chain with the right lenght of the fibers.

same observable measured using the position of the two maximums inside the integrals' range are compatible.

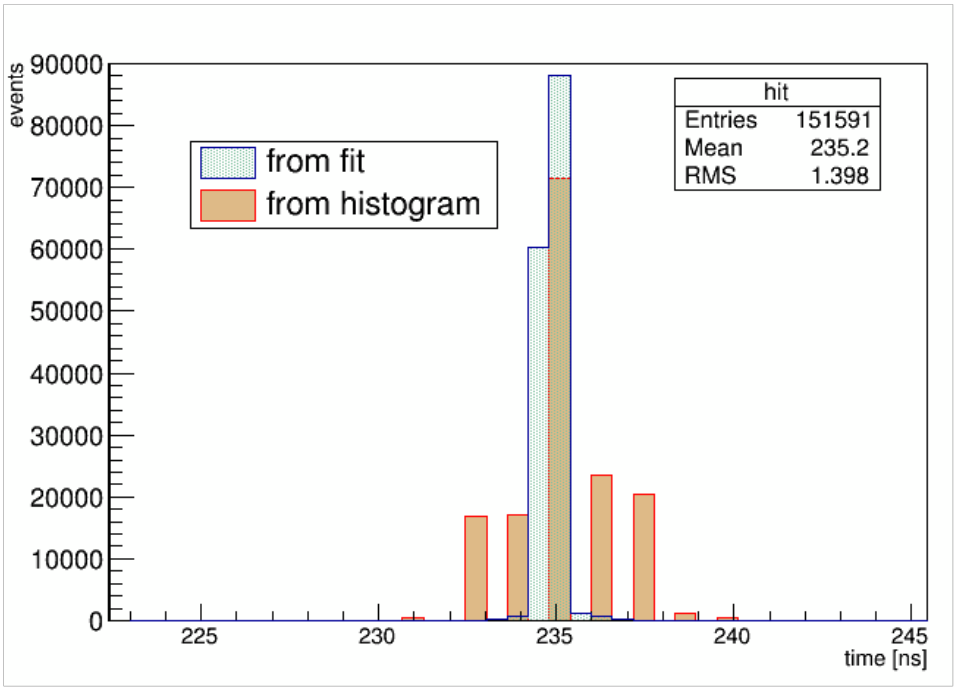

Figure 4.3.9: Time difference between the two segnals arriving to the LM

4.3.3 Stability Measurements

The stability of the light from the source to the calorimeters through the optical chain could be checked looking at the runs with a 100%-trasmittance filter. We first looked at the stability inside a run of 3 minutes, as shown in figure 4.3.10. Each point of figure 4.3.10 shows the avarage ratio between L_{CAL} and L_{SM} inside a 700 μs fill normalized respect to the first fill. The ratio normalized is a measure of the fluctuations in the light distribution chain:

$$fluctuation(t) = \frac{L_{CAL}(t)/L_{SM}(t)}{L_{CAL}(0)/L_{SM}(0)} \tag{4.3.6}$$

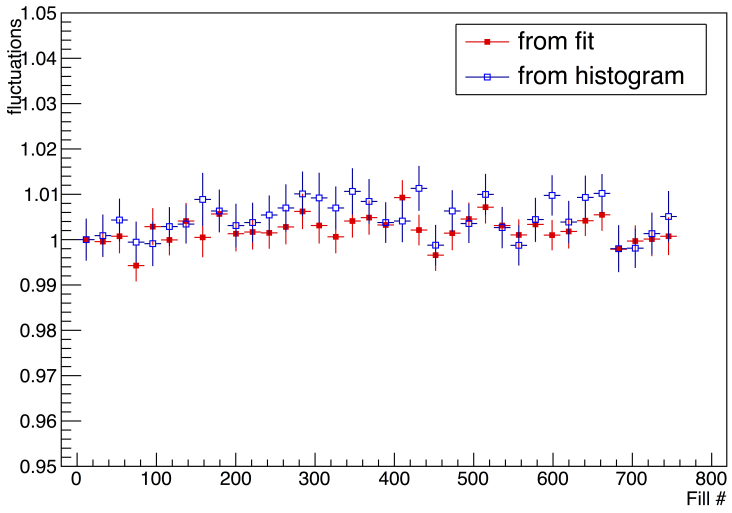

Figure 4.3.10: Stability plot inside a run of 3 minutes.

We also looked at the stability during 1.5 h of data-taking. This is shown in figure 4.3.11. Each point is the avarage fluctuation inside a ~ 7 minutes run. Fluctuations are measured with a precision of about 0.05% in approximately 7 min, so that correcting for their effects leads an uncertainty at the per-mill level, which is the precision goal for the monitoring system. Figures 4.3.10 and 4.3.11, show also that the two methods used to measure the fluctuations, *i.e.*, ratio of integrals and ratio of template's areas, give similar results within uncertainties.

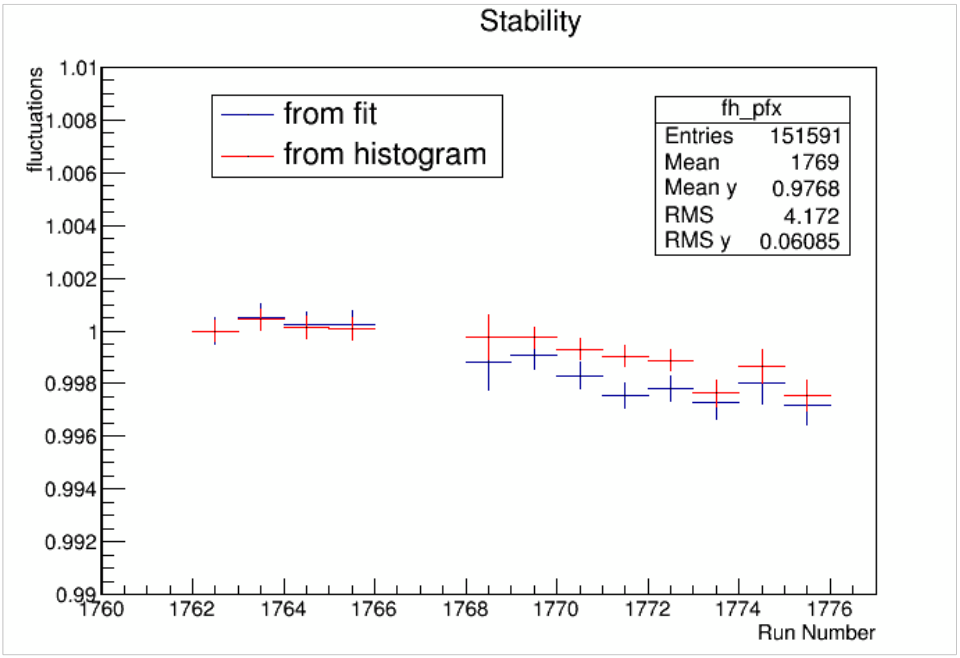

Figure 4.3.11: Overall stability: the best result I was able to obtain is a stability plot during 1.5 hours of data taking. Future measures and analysis will be necessary to have a complete overview of the system stability.

Chapter 5

Possible contributions to a_μ from New Physics

Althought the Standand Model(SM) is very well established as a renormalizable Quantum Field Theory and describes experimental data of laboratory and collider experiments, it is well established that SM is not able to explain several fundamental facts. The SM fails to account for the existence of non baryonic cold dark matter (almost 10% is normal baryonic matter), the matter-antimatter asymmetry in the universe, the problem of the cosmological constant and so on. A complete theory should include the 4th force of gravity in a natural way and explain the difference between the weak and the Planck scale.
If we confront an accurately predictable observable with a sufficiently precise measurement of it, we should be able to see that ur theory is incomplete.
The anomaluos magnetic moment of the muon provides one of the most precise tests of Quantum Field Theroy as a basicframework of elementary particle theory and of QED and the electroweak SM in particular.The comparison of theoretical and experimental values for a_μ is interesting, regardless of the outcome. If the values differ, then the comparison provides evidence for physics beyond the Standard Model. If they agree, then the result constrains between different varieties of New Physics. Some of the most important consequences of this values difference will could be:

- Muon compositeness;
- Supersymmetric loop effects;
- Existence of an Electric Dipole Moment (EDM);

Chapter 6

Conclusions

To sum up, I can say that I am pretty satisfied about the work done these two months and presented in this report. I was able to touch with hand the real job of a physicist researcher being involved in the harware and in the software part. About the hardware part I have been involved in the assemblance of the laser calibration system. The majority of the setup is now ready to future uses.
About the software I performed a complete analysis of a subset of the LM data. The main challenge was the presence of background noise so that I compared numerous methods to subtract it. It was very stimulating and interesting because even if I did the same analysis several times, every time the challenge was the improvement of the last results. The analysis is not ultimated and future prospective of this work is analyzing the entire data available.

Bibliography

[1] F. Gray [Muon $g-2$ Collaboration],
"Muon $g-2$ Experiment at Fermilab"
arXiv:1510.00346 [physics. ins-det].

[2] A.Anastasi *et al.*[Muon $g-2$ Collaboration], *"Test of candidate light distributions for the muon ($g-2$) laser calibration system"*, Nucl. Instrum. Meth. A**788**,43 (2015)
doi:10.1016/j.nima.2015.03.071
arXiv:1504.00132v1[physics.ins-det]

[3] A.T.Fienberg *et al.*, *"Studies of an array of PbF_2Cerenkov crystals with large-area SiPM readout"*, Nucl. Instrum. Meth. A **783**, 12 (2015)
doi:10.1016/j.nima.2015.02.028
arXiv:1412.5525v2 [physics.ins-det], 19 Feb 2015

[4] A.Anastasi *et al.*, *"Electron beam test of key elements of the laser-based calibration system for the muon $g-2$ experiment"* to be submitted to Nucl. Instrum. Meth. A

[5] F. Jegerlehner and A.Nyffeler *"The Muon g-2"*, Phys. Rept. **477**, 1 (2009)
doi:10.1016/j.physrep.2009.04.003
arXiv:0902.3360 [hep-ph]

[6] E. Rossi *The laser calibration system of the muon g-2 experiment at Fermilab*, Master thesis (Roma Tre U.)